Appl Intell (2009) 30: 3–23
DOI 10.1007/s10489-007-0072-0

# Classification of atherosclerotic carotid plaques using morphological analysis on ultrasound images

**E. Kyriacou · M.S. Pattichis · C.S. Pattichis · A. Mavrommatis · C.I. Christodoulou · S. Kakkos · A. Nicolaides**

Published online: 17 July 2007


**Abstract** The aim of this study was to investigate the usefulness of multilevel binary and gray scale morphological analysis in the assessment of atherosclerotic carotid plaques. Ultrasound images were recorded from 137 asymptomatic and 137 symptomatic plaques (Stroke, Transient Ischaemic Attack (TIA), Amaurosis Fugax (AF)). We carefully develop the clinical motivation behind our approach. We do this by relating the proposed $L$-images, $M$-images and $H$-images in terms of the clinically established hypoechoic, isoechoic and hyperechoic classification.

Normalized pattern spectra were computed for both a structural, multilevel binary morphological model, and a direct gray scale morphology model. From the plots of the average pattern spectra, it is clear that we have significant differences between the symptomatic and asymptomatic spectra. Here, we note that the morphological measurements appear to be in agreement with the clinical assertion that symptomatic plaques tend to have large lipid cores while the asymptomatic plaques tend to have small lipid cores.

The derived pattern spectra were used as classification features with two different classifiers, the Probabilistic Neural Network (PNN) and the Support Vector Machine (SVM). Both classifiers were used for classifying the pattern spectra into either a symptomatic or an asymptomatic class. The highest percentage of correct classifications score was 73.7% for multilevel binary morphological image analysis and 66.8% for gray scale morphological analysis. Both were achieved using the SVM classifier. Among all features, the $L$-image pattern spectra, that also measure the distributions of the lipid core components (and some non-lipid components) gave the best classification results.

E. Kyriacou (✉) · C.S. Pattichis · A. Mavrommatis · C.I. Christodoulou · A. Nicolaides
Department of Computer Science, University of Cyprus, 75 Kallipoleos Str., P.O. Box 20537, 1678 Nicosia, Cyprus
e-mail: ekyriac@ucy.ac.cy

C.S. Pattichis
e-mail: pattichi@ucy.ac.cy

A. Mavrommatis
e-mail: Andreas.mavrommatis@itd.bankofcyprus.com

C.I. Christodoulou
e-mail: cschr2@ucy.ac.cy

A. Nicolaides
e-mail: anicolai@cytanet.com.cy

E. Kyriacou
Frederick Institute of Technology, Limassol, Cyprus

E. Kyriacou · C.I. Christodoulou
Cyprus Institute of Neurology and Genetics, Nicosia, Cyprus

M.S. Pattichis
Department of Electrical and Computer Engineering, University of New Mexico, Albuquerque, USA
e-mail: pattichis@ece.unm.edu

S. Kakkos · A. Nicolaides
Department of Vascular Surgery, Faculty of Medicine, Imperial College, University of London, London, UK

S. Kakkos
e-mail: s.kakkos@imperial.ac.uk

A. Nicolaides
Vascular Screening and Diagnostic Centre, Nicosia, Cyprus

## 1 Introduction

High-resolution ultrasound has made possible the noninvasive visualization of the carotid bifurcation and for that reason it has been extensively used in the study of arterial wall changes; these include measurement of the thickness of the

intima media complex (IMT), estimation of the severity of stenosis due to atherosclerotic plaques and plaque characterization [1].

During the last decade, the introduction of computer aided methods and image standardization has improved the objective assessment of carotid plaque echogenicity, and heterogeneity [2], and has largely replaced subjective (visual) assessment [1], that had been criticized for its relatively poor reproducibility [3].

Previous studies investigated the usefulness of texture analysis [4–8], and more recently, multiscale binary morphological analysis was also used [6–9] towards the development of a Computer Aided Diagnostic (CAD) system for the classification of asymptomatic and symptomatic atherosclerotic plaques. These studies gave promising results.

In this study, we investigate the use of morphological analysis in the aforementioned classification, and compare the findings with other studies. Morphological analysis provides us with geometric methods for investigating multiresolution decompositions of the plaques. We derive our multiresolution decompositions based on structural models of the plaque (see Sect. 3.1). We also investigate a direct, morphological gray scale analysis of the plaques, and show that the structural model offers the best results. We provide a detailed clinical motivation for our study in Sect. 1.2.

The paper is structured as follows; Sect. 2 describes the material, image acquisition, normalization and segmentation of plaque images. Sections 3 and 4 describe the morphological analysis methods and the classification algorithms, respectively. Section 5 gives the results and Sect. 6 the concluding remarks.

### 1.2 Motivation

In this section we provide clinical motivation for our study. For a summary of the related medical literature on the use of ultrasound imaging in the assessment of stroke we refer to [8]. In what follows, we will provide a brief overview to help motivate our study.

In the medical literature, plaques are characterized in terms of their average echodensity level and uniformity [10]. Here, echodensity refers to the reflection of the acoustic waves through the different portions of the plaque. Thus, hypoechoic regions refer to weakly reflecting regions that appear echolucent or black. To establish that a region is hypoechoic it needs to be compared to the blood regions of the image. Similarly, isoechoic regions are established through comparison with sternomastoid. To establish that a region is hyperechoic, it needs to be compared to bone regions. Hyperechoic regions are echogenic and thus appear white in the ultrasound images. According to the uniformity of the echodensity of the plaques we have homogeneous and heterogeneous plaques [11]. It is important to note that a plaque can be homogeneous and hypoechoic, isoechoic or hyperechoic. For example, a heterogeneous hypoechoic plaque is a dark plaque characterized by non-uniform blobs.

Using natural history studies, it was suggested by Reilly [12] and confirmed by Johnson et al. in [13] that echolucent (dark) heterogeneous plaques (confirmed for 75% stenosis) will be at an increased risk of future strokes. Similarly, Langsfeld [14] confirmed that patients with hypoechoic plaques had a twofold increase in the risk of stroke (15% versus 7%). More recently, Polak et al showed that hypoechoic plaques (dark) had a significantly increased relative risk factor at 2.78 over isoechoic and hyperechoic plaques [15]. As we shall see in our discussion section (Sect. 5.3), these clinical studies are in strong agreement with our own findings that we report (for the first time) in this paper. Classification using morphological pattern spectra of the hypoechoic (low-intensity) components gave the highest possible classification yield than any other texture feature or any other component.

Beyond the use of the average intensity level, AbuRahma [16] reported a significant increase in the incidence of ipsilateral strokes in patients with heterogeneous plaques with carotid stenosis (13.6% versus 3.1% for $p = 0.0001$). In his study, he defined plaques as heterogeneous if they are composed of a mixture of hypoechoic, isoechoic and hyperechoic components. Else, if a plaque only contained a single type of components, it was classified as homogeneous. Similarly, Sterpetti [17] showed that stenosis (>50%) and heterogeneity were both independent risk factors for the development of new neurological events.

Histological studies have also provided us with significant insight into what makes plaques become unstable. We know that stable atherosclerotic plaques are characterized by a thick fibrous cap, a small lipid core, richness in smooth muscle cells (SMC) that produce collagen, with few macrophages. On the other hand, unstable plaques that are prone to rupture are characterized by a thin fibrous cap, a large lipid core, with few smooth muscle cells, and a large number of macrophages [18]. Thus, as expected, the presence of large lipid concentrations are associated with instability. We will return to this point in our discussion of the results.

In our own research, we have focused our efforts on the use of multi-feature multi-classifier systems that can be used to predict whether a plaque will become symptomatic or asymptomatic. To help establish a connection with the medical literature, we developed an image normalization method using blood and adventitia [19]. Thus, we applied histogram stretching with blood set at zero and adventitia set at 190 (out of a maximum of 255). This led to a significant reduction of inter and intra-observer variability [20, 21].

Compared to our previous attempts at classifying symptomatic versus asymptomatic plaques [6–9], the current paper reports on the most comprehensive comparative study

where we establish a correspondence between multi-level morphology and the use of hypoechoic, isoechoic and hyperochoic plaque classifications. In what follows, low-image, middle-image and hi-image correspond to hypoechoic, isoechoic and hyperechoic image components. Besides the visible correspondence, it is important to note that we have not yet established clinical equivalence (that would have required histological studies). Furthermore, for measuring homogeneity and heterogeneity, we propose the use of morphological pattern spectrum as a non-subjective measure.

In contrast to multi-level morphology, grey-scale morphology provides for a method to characterize heterogeneity that depends on the inter-relationships of hypoechoic, isoechoic and hyperechoic components. Clinically, as we have already discussed, this approach was used by AbuRahma who classified plaques as heterogeneous if they were composed of a mixture of hypoechic, isoechoic and hyperechoic components [16]. This characterization cannot be captured using multi-level morphological methods since image analysis is performed on each one of the components separately (as we discuss later).

Our prior research was primarily focused on the use of texture features and gray-level morphological methods. In this paper, for the first time, we provide a detailed mathematical characterization of the pattern spectra components. We also give comprehensive comparisons between grayscale morphology, multi-level morphology and texture features on the same data sets, with the application of the decision trees algorithm for combining features (the application is also new). Furthermore, none of our previous comparisons reported on the specificity and sensitivity of our classifiers (or the number of false positives and false negatives). No significant attempt was made at relating the findings with the related medical literature. Also, as we shall later discuss, the paper will demonstrate (for the first time) that by simply using low-image pattern spectra, we can provide superior classification performance with a system that is significantly simpler than the multi-feature multi-classifier systems in our prior work. These results are new.

## 2 Material: image acquisition, normalization and segmentation

A total of 274 carotid plaque ultrasound images (137 asymptomatic plaques and 137 symptomatic plaques) associated with retinal or hemispheric symptoms (33 stroke, 60 TIA, and 44 AF). Patients with cardioembolic symptoms or distant symptoms (>6 months) were excluded from the study. Asymptomatic plaques were truly asymptomatic if they had never been associated with symptoms in the past where as symptomatic if they had been associated with retinal or hemispheric symptoms (Stroke, TIA or AF), i.e. unstable plaques.

The ultrasound images were collected in the Irvine Laboratory for Cardiovascular Investigation and Research, Saint Mary's Hospital, UK, using an ATL (model HDI 3000—Advanced Technology Laboratories, Seattle, USA) duplex scanner with a linear broadband width 4–7 MHz (multifrequency) transducer, at approximately a resolution of 20 pixels/mm.

The gray scale images (gray levels 0–255) were normalized manually by adjusting the image linearly so that the median gray level value of blood was in the range of 0–5, and the median gray level of adventitia (artery wall) was in the range of 180–190 [21]. This normalization (i.e. using blood and adventitia as reference points) was necessary in order to extract comparable measurements in case of processing images obtained by different operators or different equipment [21].

The plaque identification and segmentation tasks are quite difficult and were carried out manually by a physician or vascular ultrasonographer who are experienced in scanning. The main difficulties are due to the fact that the plaque edges cannot be distinguished from blood based on brightness level difference, or using only texture features, or other measures. Also calcification and acoustic shadows make the problem more complex. Thus, acoustic shadows were excluded. A system for facilitating the automated segmentation of carotid plaques based on snakes is currently under development by our group [22].

## 3 Morphological analysis

Morphological features are motivated from the need to study the basic structure of the plaque. We use two morphological analysis methods in order to quantify morphological features of the plaques. The first one is based on a multilevel approach where the image intensity is thresholded at three different levels, while the second one is based on gray scale morphological analysis.

Morphological features of plaques are strongly associated with events. For example black (echolucent) plaques with white big blobs are considered to be very dangerous. From a structural perspective, morphological methods allow us to provide size distributions for different components of the plaque. We provide a more detailed discussion on the relationship between morphological methods and clinical expectations in Sect. 3.1.

We will next provide a mathematical description of the Pattern Spectrum. In developing the mathematical description, our attempt is to provide an intuition into what the Pattern Spectrum is measuring and how the measurements relate to plaque image analysis. Our presentation is closely related to previously published work in [23, 24].

Pattern spectra are defined in terms of translations and dilations of a single structural element. For the morphological analysis carried out in this research we consider the cross '+' structural element. The cross structural element exhibits limited directional selectivity. This is desirable since there is no clearly preferred direction for the analysis. We let the set $B$ to represent the '+' structural element, and define it by its five pixel coordinates

$$B = \{(-1, 0), (0, 0), (1, 0), (0, -1), (0, 1)\}. \quad (1)$$

We define discrete-set translation by points using

$$B + p = \{(m + i, n + j) : (m, n) \in B\},$$
$$\text{where } p = (i, j). \quad (2)$$

In $B + p$, we are centering the structural element over the point $p = (i, j)$. We define binary dilation using

$$X \oplus B = \bigcup_{p \in B} X + p = \{a + b : a \in X \text{ and } b \in B\}. \quad (3)$$

The definition leads to the definition of $kB$ that denotes the $k$-fold expansion of $B$, and is given by

$$kB = \begin{cases} \{(0, 0)\}, & k = 0, \\ \underbrace{B \oplus B \oplus \cdots \oplus B}_{k-1 \text{dilations}}, & \text{for integer } k > 1. \end{cases} \quad (4)$$

Pattern spectra are defined in terms of openings and closings with $kB$. We do not have any clear clinical interpretation for the pattern spectra generated by closings with $kB$. Thus, we will only focus on the pattern spectra generated by openings with $kB$. In what follows, we provide detailed descriptions of the two morphological methods in Sects. 3.1 and 3.2. In Sect. 3.3, we provide a summary of how the two methods were applied.

### 3.1 Multilevel binary morphological analysis

In multilevel binary morphological analysis we are interested in extracting different plaque components and investigating their geometric properties. We begin by generating three binary images by thresholding:

$$L = \{(i, j) \text{:such that } f(i, j) < 25\},$$
$$M = \{(i, j) \text{:such that } 25 \leq f(i, j) \leq 50\}, \quad (5)$$
$$H = \{(i, j) \text{:such that } f(i, j) > 50\}.$$

Here, binary image outputs are represented as sets of image coordinates where image intensity meets the threshold criteria. Overall, this multilevel decomposition is closely related to a three-level quantization of the original image intensity. To see this, note that we can simply assign quantization levels to each of the pixels in $L$, $M$, $H$ and then use them to provide an approximate reconstruction of the original image.

In $L$, we want to extract dark image regions representing blood, thrombus, lipid or haemorrhage. Similarly, in $H$, we want to extract the collagen and calcified components of the plaque, while in $M$, we want to extract image components that fall between the two. Thus, to decide the threshold levels of (5), we varied the threshold levels so as to extract the desired components from the plaques.

In what follows, we introduce the use of morphological pattern spectra for analyzing the extracted binary images. Our motivation lies in analyzing the structural components of each binary image. We provide a few examples motivated by clinical (visual) observations (see Sect. 1.2 for a more detailed discussion).

Note that if the plaque is captured as a single component in the high intensity image ($H$), then the plaque is most likely to be stable with little chance for rupture. This comes from the fact that such plaques can be characterized as homogeneous with calcified or collagen components (also see Sect. 1.2). Also, the plaque will most likely be asymptomatic if the lipid core regions in the low intensity image are made up of small, scattered components. The most dangerous cases occur when image components in the middle image ($M$) appear to be very thin. The risk may be less when image components in the middle image appear relatively thick. This expectation assumes that the thin components represent a thin fibrous cap, a well known characteristic of unstable plaques (see Sect. 1.2).

We also expect that black (echolucent) plaques with white big blobs to be very dangerous. In this case, we would expect to see large components in both the low image and the high image intensity images (see Fig. 1). These plaques can be characterized as heterogeneous with large lipid cores.

We compute normalized pattern spectra for each one of the three binary images $L$, $M$, $H$. Thus, in the following discussion, we will use the symbol $X$ to denote any one of the three binary images $L$, $M$, $H$. Binary image erosion is defined using

$$X \odot B = \bigcap_{p \in B} X - p = \{a : B + a \subseteq X\}. \quad (6)$$

An opening is then defined in terms of an erosion followed by a dilation:

$$X \circ B = (X \odot B) \oplus B. \quad (7)$$

In general, an opening reduces the input image $X \odot B \subseteq X$. However, when the input image can be expressed in terms of translations of the structural element $B$, the opening operation will preserve the input image. We thus write

$$X \circ B = X \quad (8)$$

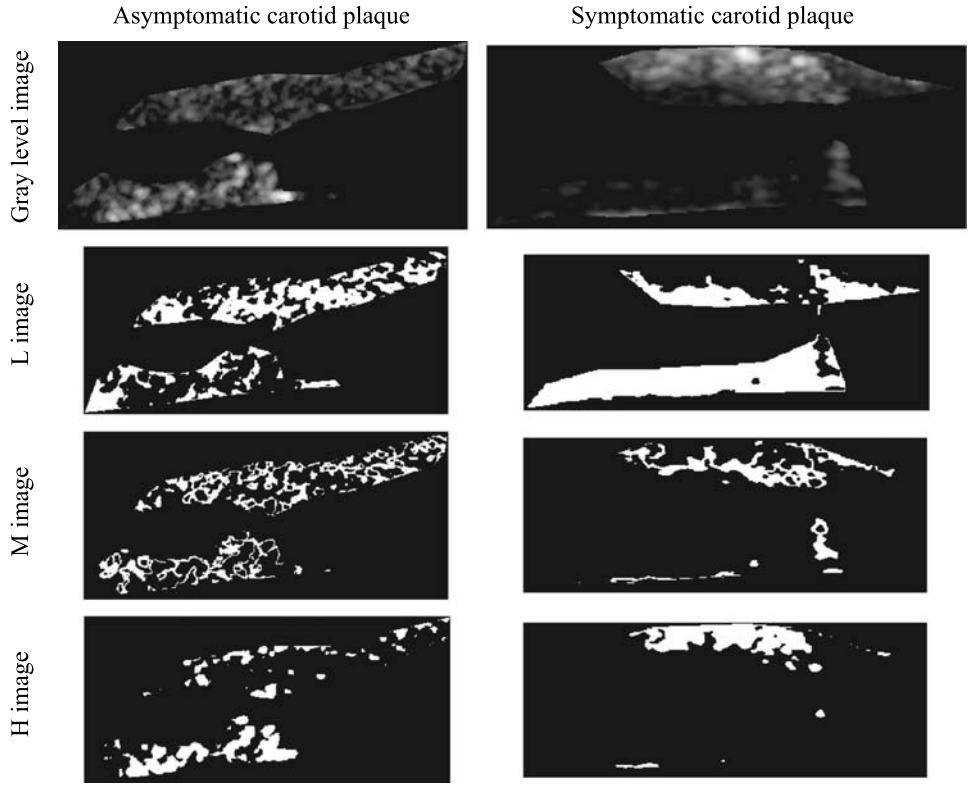


**Fig. 1** The three binary level images: $(L, M, H)$ of an asymptomatic and a symptomatic carotid plaque

when

$$X = \bigcup_{p \in S} B + p = B \oplus S = S \oplus B \tag{9}$$

for some set of possible translates $S$. This follows from ([24], see (10)). From (8–9), we note that an opening will not alter the binary input image provided that the binary image components are "thick and rough enough" to contain all translates of the structural element. On the other hand, any isolated components of $X$ that are smaller than $B$ will be removed by the opening operation. Here, we define smaller in terms of set operations. We say that a binary image set $A$ is smaller than another binary image set $B$ if $A$ is a proper subset of a translation of $B$. Conversely, any isolated components of $X$ that are larger than $B$ will not be totally removed from the opening operation (where larger is defined in a similar way).

In general, for any given binary image, an opening outputs an approximation to the input image. This approximation is expressed as a union of translations of the structural element [24]:

$$X \circ B = \bigcup_{B+z \subseteq X} B + z. \tag{10}$$

The approximation error image is defined in terms of the set difference $X - X \circ B$. We quantify the approximation error by counting the number of pixels in the difference image. We write $A(S)$ to denote the cardinality of the set $S$.

For measuring the binary components at different scales, we consider a sequence of openings with the dilated structural element (see (4)):

$$X, X \circ B, X \circ 2B, \ldots, X \circ nB. \tag{11}$$

For our plaque images, we note that the plaques are segmented, and image intensity outside the plaque is assigned to zero (see Fig. 1). Thus, for a sufficiently large value of $k$, $kB$ will outgrow the support of the plaque. When this happens, the opening operation will return the empty-set image. We thus pick $n$ to be the smallest integer for which $X \circ (n+1)B = \emptyset$.

For computing (11), we note that a single opening is needed each time, since the openings can be computed recursively using $X \circ (n+1)B = (X \circ nB) \circ B$. It is also clear from this recursive relationship that the openings generate decreasing images

$$X \circ nB \subseteq \cdots \subseteq X \circ 2B \subseteq X \circ B \subseteq X \tag{12}$$

with decreasing areas

$$A(X \circ nB) \leq \cdots \leq A(X \circ 2B) \leq A(X \circ B) \leq A(X). \tag{13}$$

We form the set difference images using

$$\begin{aligned} d_0(X;B) &= X - X \circ B, \\ d_1(X;B) &= X \circ B - X \circ 2B, \\ &\vdots \\ d_{n-1}(X;B) &= X \circ (n-1)B - X \circ nB. \end{aligned} \tag{14}$$

The difference images are orthogonal with respect to set intersection

$$d_i(X;B) \cap d_j(X;B) = \emptyset \quad \text{when } i \neq j. \tag{15}$$

We can reconstruct the image using the difference images

$$\begin{aligned} X &= (X \circ nB) \cup \left( \bigcup_{i=0}^{n-1} d_i(X;B) \right) \\ &= \bigcup_{i=0}^{n} d_i(X;B). \end{aligned} \tag{16}$$

We think of the image decomposition given by (16) as a multiscale decomposition where the difference images $d_i(f;B)$ represent information captured at the $i$-th scale.

The pattern spectrum is also defined in terms of the number of elements in the difference images

$$PS_X(n,B) = A(d_n(X;B)). \tag{17}$$

In (17), we note that the pattern spectra vary with the size of the plaque.

To remove this dependency, we consider a probability density function (*pdf*) measure defined as

$$pdf_X(k,B) = A(d_k(X;B))/A(X) \quad \text{for } k \geq 0. \tag{18}$$

In (18), we note that the normalization is motivated by the reconstruction formula (see (16)). Given the *pdf*-measure, we can also construct the cumulative distribution function (*cdf*) using

$$cdf_f(k,B) = \begin{cases} 0, & k = 0, \\ \sum_{r=0}^{k-1} pdf_f(r,B), & n+1 \geq k > 0. \end{cases} \tag{19}$$

### 3.2 Gray scale morphological analysis

For gray scale morphological analysis, we assume that the input image $f(i,j)$ denotes the (positive) gray scale image intensity at pixel $(i,j)$. At every pixel, for structural element $B$, we define gray scale dilation by

$$(f \oplus B)(i,j) = \max_{(m,n) \in B+(i,j)} f(m,n) \tag{20}$$

which represents the maximum intensity value over the support of the translated structural element. Similarly, for symmetric structural elements (as is the case for '+'), we define gray scale erosion using the minimum value:

$$(f \odot B)(i,j) = \min_{(m,n) \in B+(i,j)} f(m,n). \tag{21}$$

We then define openings using the new definitions for grey-scale erosions and dilations. Instead of the subset relation, we now have that an opening reduces image intensity in the sense that $f \circ B \leq f$ for every pixel.

Due to the bounds of the extend of the plaque, we are again limited in the maximum number of openings that make sense. Here, instead of the empty set, the limit is the zero-image. The difference images are formed in the same way. For the reconstruction, we use a finite sum instead of a union:

$$\begin{aligned} f &= (f \circ nB) + \left( \sum_{i=0}^{n-1} d_i(f;B) \right) \\ &= \sum_{i=0}^{n} d_i(f;B). \end{aligned} \tag{22}$$

For the gray scale definition of the pattern spectrum we use

$$PS_f(k,B) = \|d_k(f;B)\|, \tag{23}$$

where

$$\|f\| = \sum_{(i,j)} f(i,j). \tag{24}$$

We then normalize by the original image intensity

$$pdf_f(k,B) = \|d_k(f;B)\|/\|f\|, \quad \text{for } k \geq 0. \tag{25}$$

### 3.3 Morphological analysis application to atherosclerotic carotid plaques

We begin with a summary. For each plaque we compute the three binary images $L$, $M$, $H$ as outlined in (5). For each binary image, we compute the *pdf* and *cdf* distributions as outlined in (18–19), for $k = 0, \ldots, 70$. Similarly, for gray scale morphological image analysis, we compute the *pdf* and *cdf* distributions based on gray scale erosions and dilations (see (25)). Thus, we compute *pdf* and *cdf* measures on the original gray scale image and the three binary images that are derived from it.

For each one of the four images, the positively-indexed *pdf* and *cdf* measures provide us with normalized size distributions of the white (or brighter) blob-components. These measures are based on binary and gray scale openings. Some examples are shown in Fig. 2. We provide a more detailed discussion in the results section.

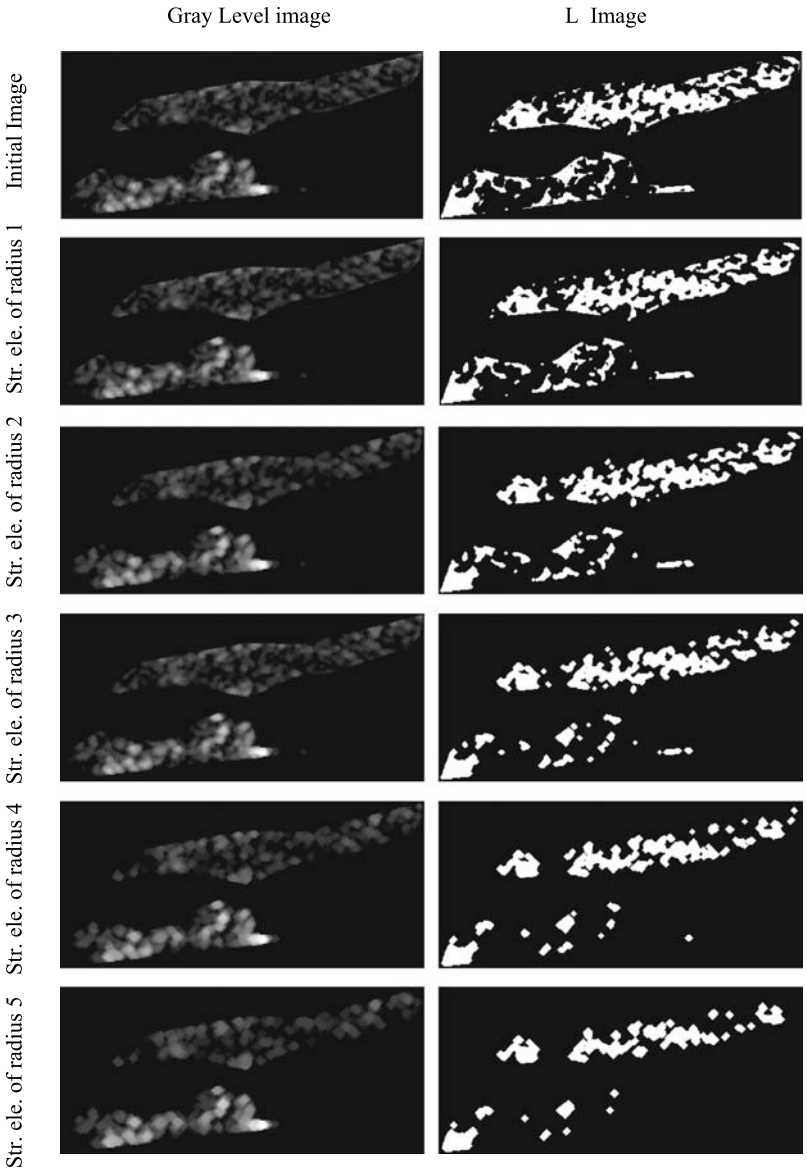


**Fig. 2** Results from a sequence of openings using a '+' structural element on a gray level and a low-intensity image ($L$-image in multi-level binary morphology) of an asymptomatic carotid plaque. The radius of the structural element ranges from 1 to 5 pixels (plotted at 20 pixels/mm)

## 4 Classification models

The diagnostic performance of the morphological features was evaluated with two different classifiers: the Probabilistic Neural Network (PNN), and the Support Vector Machine (SVM). These classifiers were trained to classify the morphology features into two classes: (i) asymptomatic plaques or (ii) symptomatic plaques associated with retinal or hemispheric symptoms (Stroke, TIA or AF), i.e. unstable plaques.

### 4.1 The PNN classifier

A Probabilistic Neural Network (PNN) classifier was used for developing classification models for the problem under study. The PNN falls within the category of nearest-neighbor classifiers [25]. For a given vector $\mathbf{w}$ to be classified, an activation $a_i$ is computed for each of the two classes of plaques ($i = 1, \ldots, 2$). The activation $a_i$ is defined to be the total distance of $\mathbf{w}$ from each of the $M_i$ prototype feature vectors $\mathbf{x}_j^{(i)}$ that belong to the $i$-th class:

$$a_i = \sum_{j=1}^{M_i} \exp[-\beta(\mathbf{w} - \mathbf{x}_j^{(i)})^T(\mathbf{w} - \mathbf{x}_j^{(i)})], \tag{26}$$

where $\beta$ is a smoothing factor. The normalized activations $\tilde{a}_i = a_i / \sum_{i=1}^{N} a_i$ provide a confidence estimate for the hypothesis that $\mathbf{w}$ belongs to class $i$. We then classify $\mathbf{w}$ into the class that yields the highest confidence. An important advantage of the PNN is that it provides confidence estimates for our classification decision. Also, to avoid dependence on the smoothing factor $\beta$, the value of $\beta$ was set to the one that

yielded the minimum misclassification error on the training set.

This classifier was investigated for several spread radii in order to identify the best radius for the current problem.

### 4.2 The SVM classifier

The Support Vector Machine (SVM) was also used for developing classification models for the problem. The method is initially based on a nonlinear mapping of the initial data set using a function $\varphi(.)$ and then the identification of a hyperplane which is able to achieve the separation of two categories of data. Details about the implementation of the SVM algorithm used can be found in [26].

The SVM network was investigated using Gaussian Radial Basis Function (RBF) kernels; this was decided as the rest of the kernel functions could not achieve satisfactory results. The SVM with RBF kernel was investigated using 10-fold cross validation in order to identify the best parameters such as the spread of RBF [26].

### 4.3 Classification tests

The leave-one-out estimate was used for validating all the classification models. A total of 274 subsets of size 273 were used for training the classifiers, and the performances of the classifiers were evaluated on the remaining one subset.

The performances of the classifier systems were measured using the receiver operating characteristics (ROC) curve parameters [27]. The parameters calculated for ROC curves are the numbers of: (i) true positives (TP) when the system correctly classifies plaques as symptomatic, (ii) false

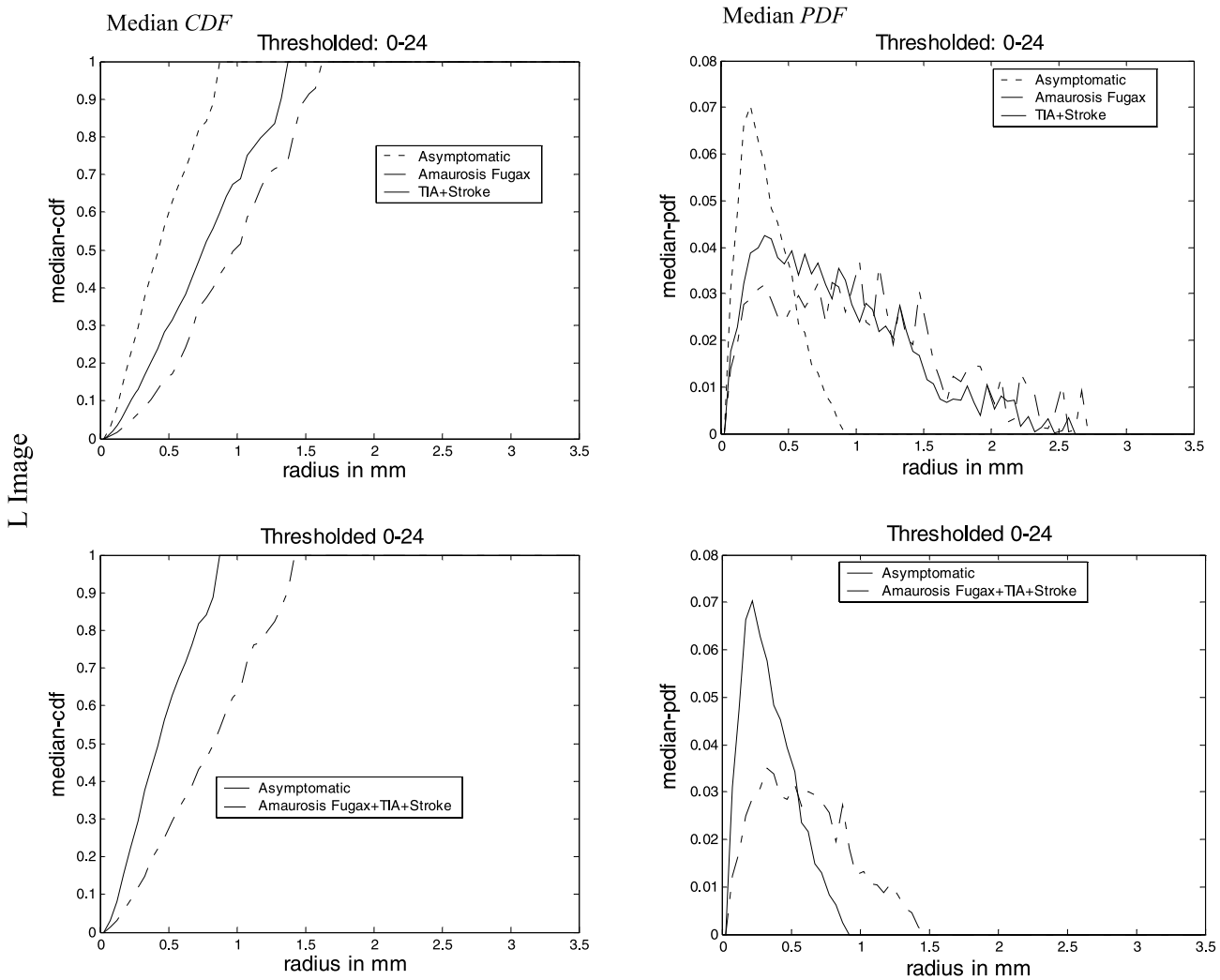


**Fig. 3** Corresponding median values of the *pdfs* and *cdfs* of asymptomatic versus symptomatic plaques for the three different levels ($L$, $M$, $H$ images) of multilevel binary morphological analysis. The *first line* of each sub-plot represents the median *cdf* and *pdf* for Asymptomatic Vs Amaurosis Fugax Vs (TIA&Stroke) plaques, while the *second line* represents the median cdf and pdf for Asymptomatic Vs Symptomatic plaques. In the plot, radius refers to radial spread of the structural element

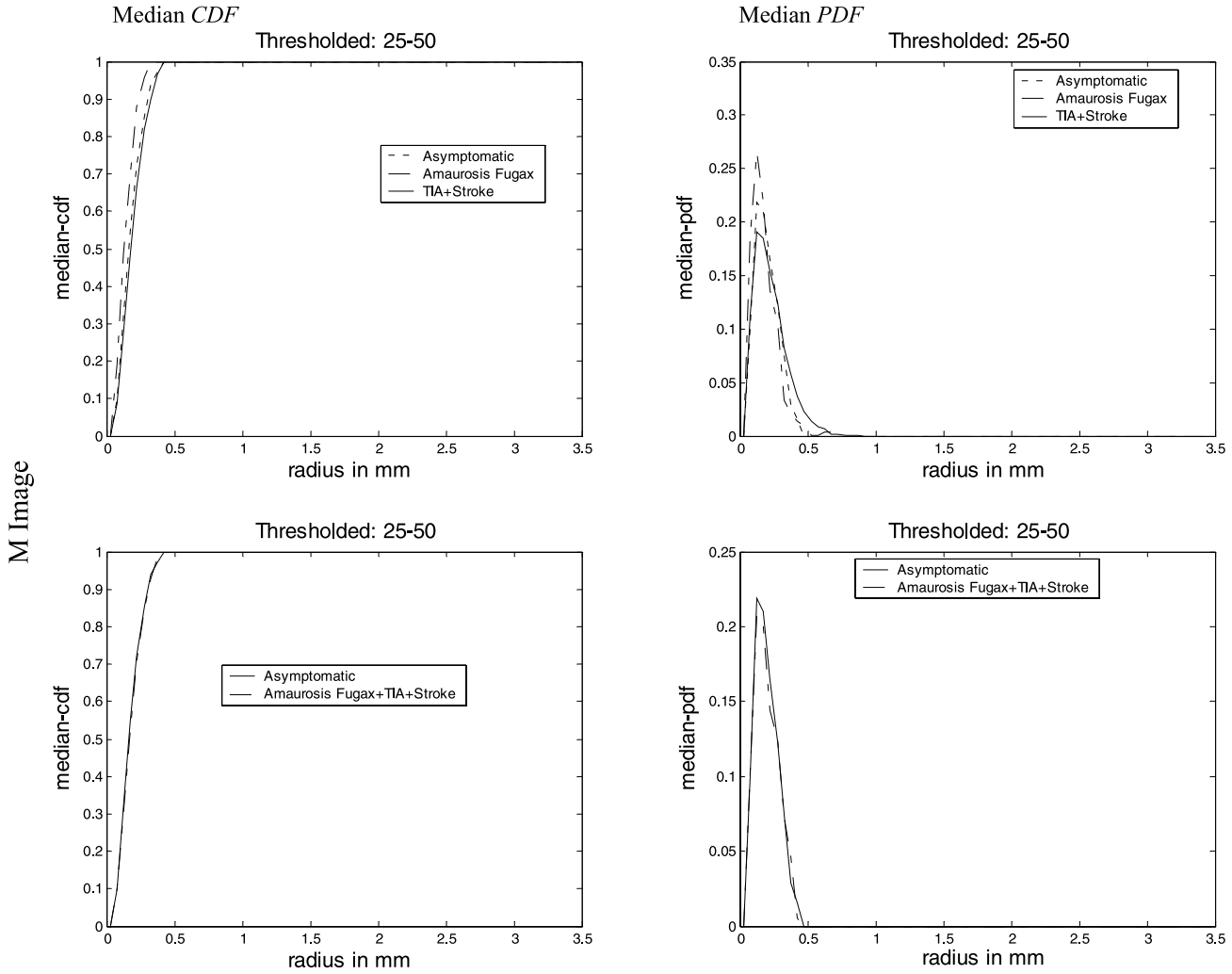


**Fig. 3** (*continued*)

positives (FP) where the system wrongly classifies plaques asymptomatic while they are asymptomatic, (iii) false negatives (FN) when the system wrongly classifies plaques as asymptomatic while they are symptomatic, and (iv) true negatives (TN) when the system correctly classifies plaques as asymptomatic. We also compute the Sensitivity (SE) which is the likelihood that a symptomatic plaque will be detected given that it is symptomatic and Specificity (SP) which is the likelihood that a plaque will be classified as asymptomatic given that is asymptomatic. For the overall performance, we provide the correct classification (CC) rate which gives the percentage of correctly classified plaques.

## 5 Results

The median of the estimated *pdfs* and *cdfs* extracted from the plaques can be seen in Figs. 3 and 4. All figures are plotted against the radial size of the structural element. We have divided the results into the two categories of multilevel binary and gray scale morphological analysis. We provide a critical discussion in Sect. 5.3.

### 5.1 Results from multilevel binary morphological analysis

From the results, we observe that the median symptomatic *cdf* is *stochastically* smaller than the median asymptomatic *cdf* for the $L$-images.This means that the median *cdf* for the symptomatic cases assumes equal or smaller values than the asymptomatic *cdf.* The median and box plots of *pdfs* and *cdfs* for $L$, $M$ and $H$ images can be seen in Figs. 5, 6, 7 respectively.

For the $M$-images, the median *cdf* of the asymptomatic cases turned out to be *stochastically* larger to that of TIA&Stroke but smaller to that of Amaurosis Fugax; thus the median *cdfs* of asymptomatic and symptomatic plaques are almost equal. Due to these observations, as expected, the

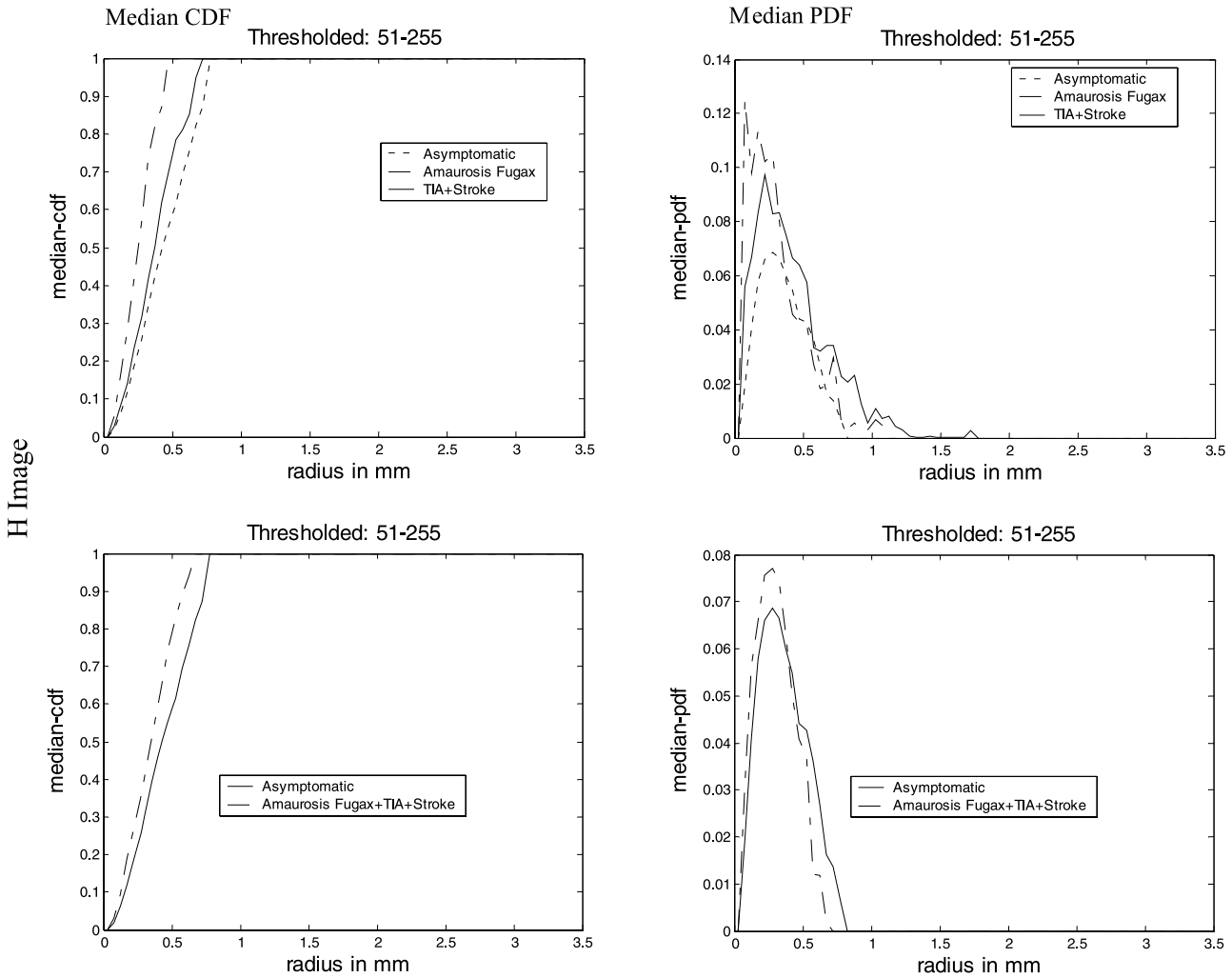


**Fig. 3** (*continued*)

classification results from the $M$-images where relatively lower. Finally, for the $H$-images, the median symptomatic *cdf* turned out to be *stochastically* larger than the asymptomatic *cdf*.

The *cdf*s and *pdf*s of all plaques were used with the PNN and SVM classifiers. Both classifiers were tested on both the *pdf* and *cdf* feature sets. The first set included features produced for the whole range of scales (1–70) while the second set included the pattern spectra of selected scales ($L$-Images: 1, 2, 3, 4, 5, $M$-Images: 3, 4, 9, 11, 12, $H$-Images: 2, 11, 12, 15, 18, also see [28, 29]). These scales were selected because of their discriminatory power as evaluated using the C4.5 decision trees algorithm [30]. The C4.5 was run and the pattern spectra scale with the highest discriminative score was computed. This best scale was then removed and the C4.5 was run again to compute the next best scale. The procedure was repeated 5 times. The dimensionality of the entire pdf/cdf feature vectors from both sets was also reduced using Principal Components Analysis (PCA). For PCA, we selected a small number of components that accounted for 98% of the total variance.

Table 1 presents the results of the ROC analysis for the SVM and PNN classifiers for the different feature sets investigated. Classifiers were tested using features extracted from the $L$, $M$ and $H$ images and the combination of the three. The highest percentage of correct classifications score was 73.7% and was achieved using the SVM classifier on the features extracted from the $L$-images (*cdf* scales: 1–70 + PCA). For PNN, the highest percentage of correct classifications score achieved was 70.4% for *pdf* scales: 1–70 + PCA. The combination of the three feature sets gave the same highest results as those achieved with the $L$-images feature set.

### 5.2 Results from gray scale morphological analysis

From the results, we can observe that the median symptomatic *cdf* is *stochastically* larger than the median asymp-

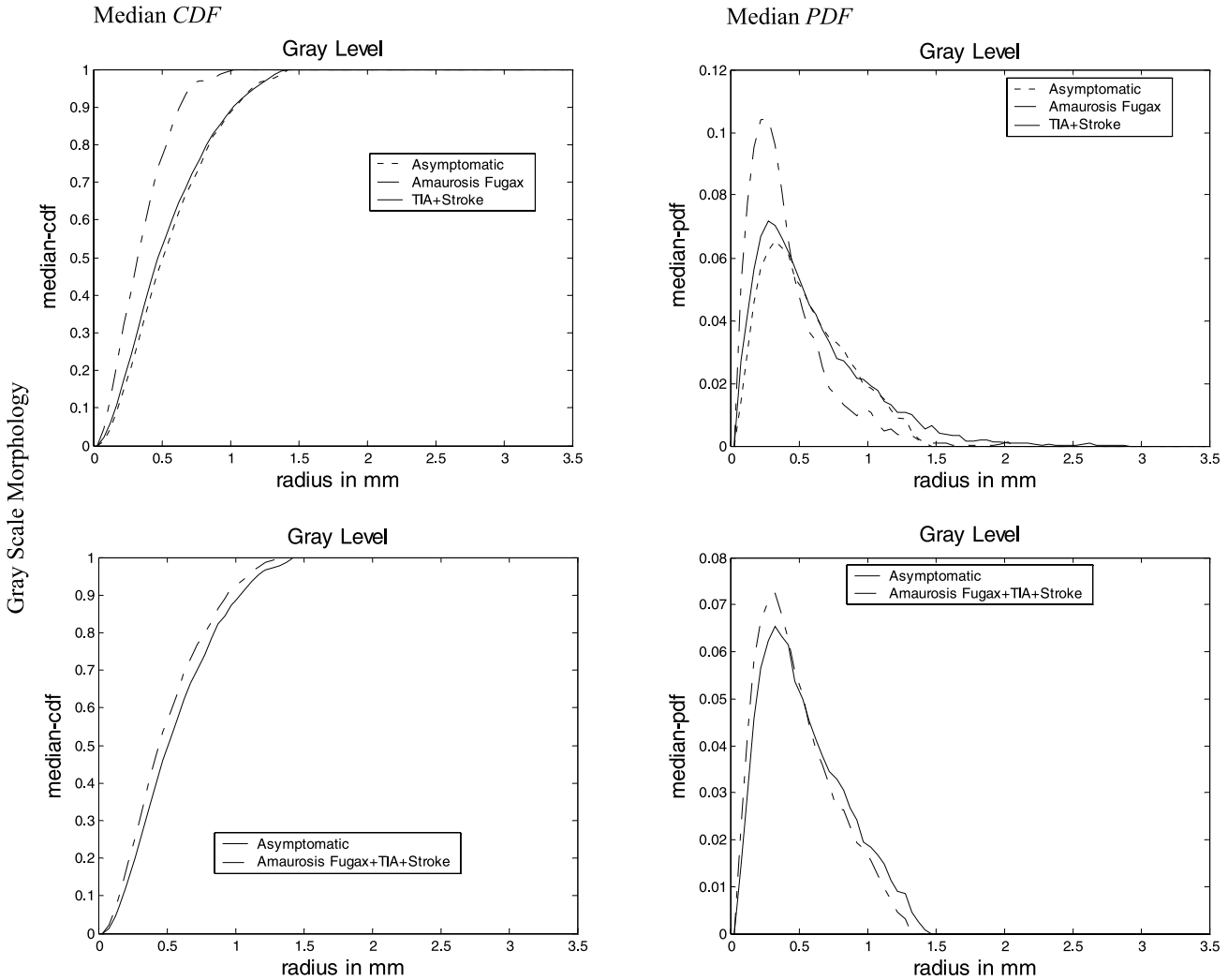


**Fig. 4** Corresponding median values of the *pdfs* and *cdfs* of asymptomatic versus symptomatic plaques for the gray scale morphological analysis. The *first row* represents the median *cdf* and *pdf* for Asymptomatic Vs Amaurosis Fugax Vs (TIA & Stroke) plaques, while the *second* represents median *cdf* and *pdf* for Asymptomatic Vs Symptomatic plaques

tomatic *cdf*. Recall that this means that the median *cdf* for the symptomatic cases assumes equal or larger values than the asymptomatic *cdf*. The median and box plots of *pdfs* and *cdfs* for gray scale morphological can be seen in Fig. 8.

Again the *cdf*s and *pdf*s of all plaques were used with the PNN and SVM classifiers. Both classifiers were tested on both the *pdf* and *cdf* feature sets. The first set included features produced for the whole range of scales (1–70) while the second set included the pattern spectra of selected scales (2, 3, 5, 10, 21, and 23) [29], using the C4.5 decision trees algorithm [30] (see Sect. 5.1)

Table 2 presents the results of the ROC analysis for the SVM and PNN classifiers for the different feature sets investigated. The highest percentage of correct classifications score was 66.7% and was achieved using the SVM classifier on the second set of data (*pdf* scales: 2, 3, 5, 10, 21, and 23 + PCA). For PNN, the highest percentage of correct classifications score achieved was 62.04% for *cdf* scales: 1–70.

### 5.3 Discussion

An important contribution of this paper is that it reports on the most successful classification results (73.7%) using the pattern-spectra from the low-image components of the plaque. Thus, in contrast with our prior work where the best results had resulted from the use of multiple features and multiple classifiers, we have found that there is virtually nothing to be gained over the use of low-image pattern spectra. We note that this finding is in strong agreement with clinical findings on the hypoechoic images (see [12–17] and our discussion in Sect. 1.2).

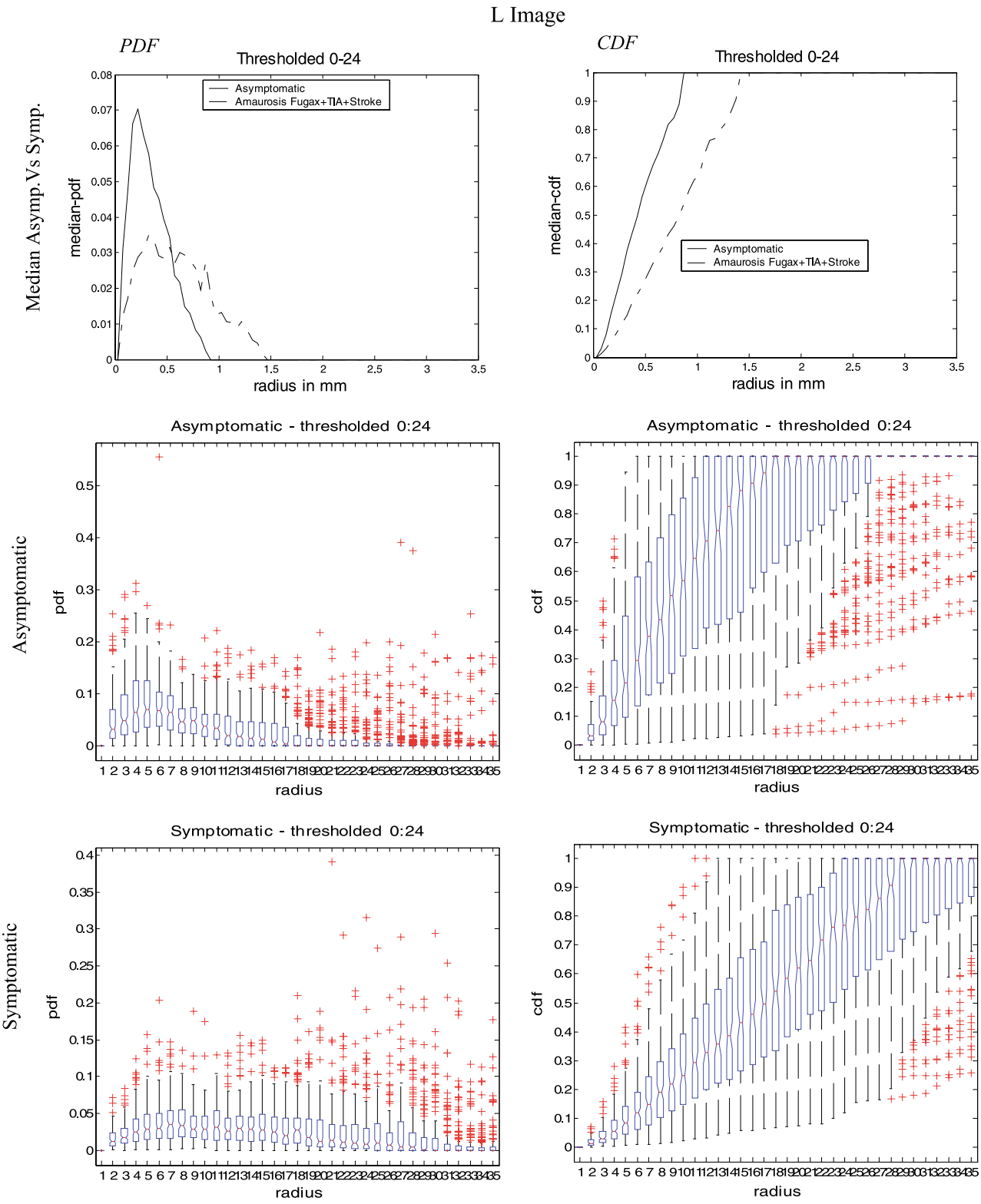


**Fig. 5** **a** Median probability density function *(pdf)* and cumulative distribution function *(cdf)* plots for the pattern spectra of the *L* images; the symptomatic plot is plotted with a *solid line* while the asymptomatic one with a *dotted line*. **b** Box plots of the *pdf* and the *cdf* for the asymptomatic carotid plaques. **c** Box plots of the *pdf* and the *cdf* for the symptomatic carotid plaques. Box plots are described as follows: The notched box shows the median, lower and upper quartiles and confidence interval around the median for each feature. The *dotted line* connects the nearest observations within 1.5 of the inter-quartile range (IQR) of the lower and upper quartiles. Crosses (+) indicate possible outliers with values beyond the ends of the 1.5 × IQR. In the plot, radius refers to the index of the normalized *pdf*s and *cdf*s (see (25))

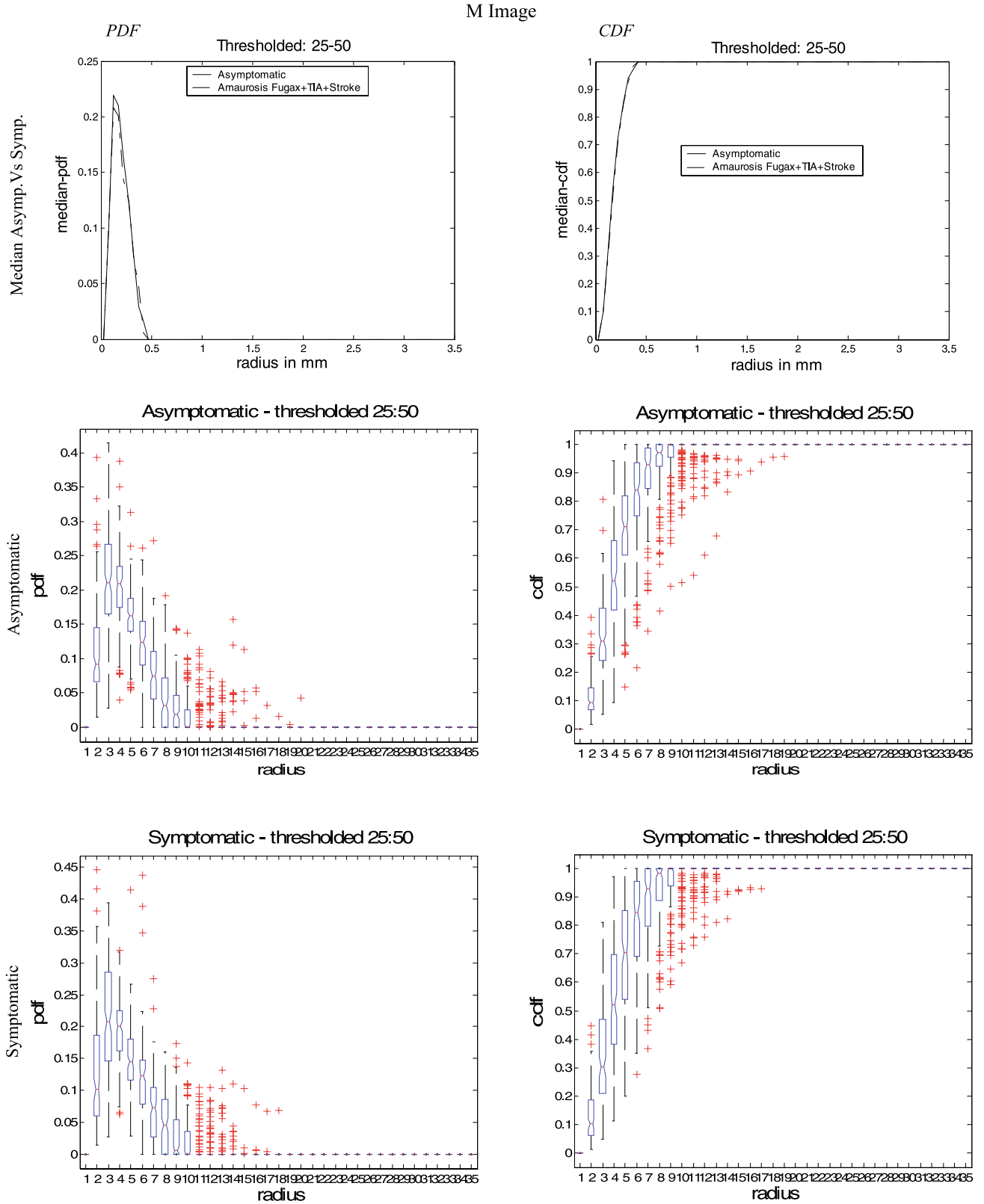


**Fig. 6** **a** Median probability density function *(pdf)* and cumulative distribution function *(cdf)* plots for the pattern spectra of the $M$-images; symptomatic plot is plotted with a *solid line* while the asymptomatic one with a *dotted line*. **b** Box plots of the *pdf* and *cdf* for the asymptomatic carotid plaques. **c** Box plots of *pdf* and *cdf* for the symptomatic carotid plaques

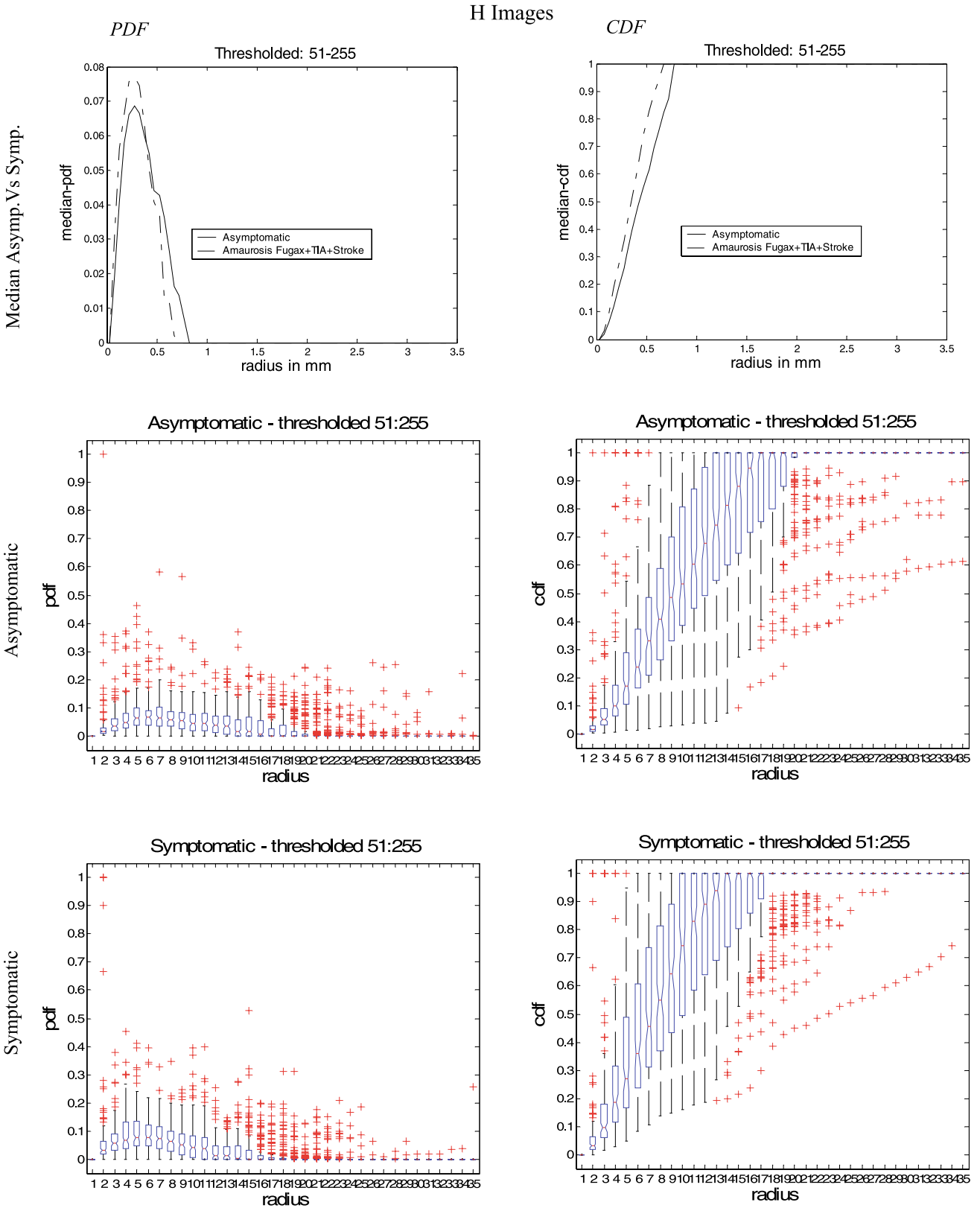


**Fig. 7** **a** Median probability density function *(pdf)* and cumulative distribution function *(cdf)* plots for the pattern spectra of the $H$-images; symptomatic plot is plotted with a *solid line* while the asymptomatic one with a *dotted line*. **b** Box plots of the *pdf* and *cdf* for the asymptomatic carotid plaques. **c** Box plots of the *pdf* and *cdf* for the symptomatic carotid plaques

**Table 1** Percentage of correct classifications (%CC), percentage of false positives (%FP), percentage of false negatives (%FN), percentage sensitivity (%SE) and percentage specificity (%SP) of Multi Level morphological features using the SVM and PNN classifiers, for the *L*, *M* and *H* images. Classification models developed for two classes using the leave one out method, with 137 symptomatic and 137 asymptomatic plaques

| L Image | | | | | |
|---|---|---|---|---|---|
| SVM classifier | %CC | %FP | %FN | %SE | %SP |
| SVM rbf spread = 0.4 | 70.80 | 42.34 | 16.06 | 83.94 | 57.66 |
| **PCA** for *pdf* scales 1,2,3,4,5,6 | | | | | |
| SVM rbf spread = 9.0510 | 69.71 | 51.09 | 9.49 | 90.51 | 48.91 |
| *pdf* scales 1,2,3,4,5,6 | | | | | |
| SVM rbf spread = 0.1 | **73.72** | **36.50** | **16.06** | **83.94** | **63.50** |
| **PCA** for *cdf* scales 1–70 | | | | | |
| SVM rbf spread = 12.8 | 72.26 | 37.23 | 18.25 | 81.75 | 62.77 |
| *cdf* scales 1–70 | | | | | |
| SVM rbf spread = 1.6 | 70.07 | 43.07 | 16.79 | 83.21 | 56.93 |
| **PCA** for *pdf* scales 1–70 | | | | | |
| SVM rbf spread = 9.0510 | 70.80 | 41.61 | 16.79 | 83.21 | 58.39 |
| *pdf* scales 1–70 | | | | | |
| **Average Values** | 71.23 | 41.97 | 15.57 | 84.43 | 58.03 |
| L Image | | | | | |
| PNN classifier | %CC | %FP | %FN | %SE | %SP |
| PNN spread = 5 | 66.79 | 62.77 | 3.65 | 96.35 | 37.23 |
| **PCA** for *pdf* scales 1,2,3,4,5,6 | | | | | |
| PNN spread = 5 | 66.79 | 63.50 | 2.92 | 97.08 | 36.50 |
| *pdf* scales 1,2,3,4,5,6 | | | | | |
| PNN spread = 5 | **70.07** | **37.96** | **21.90** | **78.10** | **62.04** |
| **PCA** for *cdf* scales 1–70 | | | | | |
| PNN spread =5 | **70.07** | **37.96** | **21.90** | **78.10** | **62.04** |
| *cdf* scales 1–70 | | | | | |
| PNN spread = 5 | **70.44** | **40.88** | **18.25** | **81.75** | **59.12** |
| **PCA** for *pdf* scales 1–70 | | | | | |
| PNN spread = 5 | 69.71 | 35.77 | 24.82 | 75.18 | 64.23 |
| *pdf* scales 1–70 | | | | | |
| **Average Values** | 68.98 | 46.47 | 15.57 | 84.43 | 53.53 |
| M Image | | | | | |
| SVM classifier | %CC | %FP | %FN | %SE | %SP |
| SVM rbf spread = 0.1414 | **60.58** | **45.99** | **32.85** | **67.15** | **54.01** |
| **PCA** for *pdf* scales 3,4,9,11,12 | | | | | |
| SVM rbf spread = 0.1 | 59.49 | 47.45 | 33.58 | 66.42 | 52.55 |
| *pdf* scales 3,4,9,11,12 | | | | | |
| SVM rbf spread = 2.2627 | 55.47 | 34.31 | 54.74 | 45.26 | 65.69 |
| **PCA** for *cdf* scales 1–70 | | | | | |
| SVM rbf spread = 0.2 | 59.12 | 29.93 | 51.82 | 48.18 | 70.07 |
| *cdf* scales 1–70 | | | | | |
| SVM rbf spread = 0.4 | 58.39 | 37.96 | 45.26 | 54.74 | 62.04 |
| **PCA** for *pdf* scales 1–70 | | | | | |
| SVM rbf spread = 0.1 | 58.39 | 37.96 | 45.26 | 54.74 | 62.04 |
| *pdf* scales 1–70 | | | | | |
| **Average Values** | 58.57 | 38.93 | 43.92 | 56.08 | 61.07 |

**Table 1** (*continued*)

| M Image | | | | | |
|---|---|---|---|---|---|
| PNN classifier | %CC | %FP | %FN | %SE | %SP |
| PNN spread = 5 | 48.18 | 10.95 | 92.70 | 7.30 | 89.05 |
| **PCA** for *pdf* scales 3,4,9,11,12 | | | | | |
| PNN spread = 5 | 48.18 | 10.95 | 92.70 | 7.30 | 89.05 |
| *pdf* scales 3,4,9,11,12 | | | | | |
| PNN spread = 5 | 49.27 | 9.49 | 91.97 | 8.03 | 90.51 |
| **PCA** for *cdf* scales 1–70 | | | | | |
| PNN spread = 5 | 48.91 | 11.68 | 90.51 | 9.49 | 88.32 |
| *cdf* scales 1–70 | | | | | |
| PNN spread = 5 | 51.46 | 9.49 | 87.59 | 12.41 | 90.51 |
| **PCA** for *pdf* scales 1–70 | | | | | |
| PNN spread = 5 | 51.09 | 9.49 | 88.32 | 11.68 | 90.51 |
| *pdf* scales 1–70 | | | | | |
| **Average Values** | 49.52 | 10.34 | 90.63 | 9.37 | 89.66 |
| H Image | | | | | |
| SVM classifier | %CC | %FP | %FN | %SE | %SP |
| SVM rbf spread = 9.0510 | 58.76 | 47.45 | 35.04 | 64.96 | 52.55 |
| **PCA** for *pdf* scales 2,11,12,15,18,19 | | | | | |
| SVM rbf spread = 12.8 | 58.39 | 47.45 | 35.77 | 64.23 | 52.55 |
| *pdf* scales 2,11,12,15,18,19 | | | | | |
| SVM rbf spread = 6.4 | 59.12 | 42.34 | 39.42 | 60.58 | 57.66 |
| **PCA** for *cdf* scales 1–70 | | | | | |
| SVM rbf spread = 0.4 | 59.12 | 41.61 | 40.15 | 59.85 | 58.39 |
| *cdf* scales 1–70 | | | | | |
| SVM rbf spread = 9.0510 | **62.04** | **40.88** | **35.04** | **64.96** | **59.12** |
| **PCA** for *pdf* scales 1–70 | | | | | |
| SVM rbf spread = 0.8 | 60.22 | 45.26 | 34.31 | 65.69 | 54.74 |
| *pdf* scales 1–70 | | | | | |
| **Average Values** | 59.61 | 44.17 | 36.62 | 63.38 | 55.84 |
| H Image | | | | | |
| PNN classifier | %CC | %FP | %FN | %SE | %SP |
| PNN spread = 5 | 43.80 | 24.82 | 87.59 | 12.41 | 75.18 |
| **PCA** for *pdf* scales 2,11,12,15,18,19 | | | | | |
| PNN spread = 5 | 43.80 | 24.82 | 87.59 | 12.41 | 75.18 |
| *pdf* scales 2,11,12,15,18,19 | | | | | |
| PNN spread = 5 | **59.12** | **48.18** | **33.58** | **66.42** | **51.82** |
| **PCA** for *cdf* scales 1–70 | | | | | |
| PNN spread = 5 | 58.76 | 48.91 | 33.58 | 66.42 | 51.09 |
| *cdf* scales 1–70 | | | | | |
| PNN spread = 5 | 57.66 | 64.23 | 20.44 | 79.56 | 35.77 |
| **PCA** for *pdf* scales 1–70 | | | | | |
| PNN spread = 5 | 55.47 | 65.69 | 23.36 | 76.64 | 34.31 |
| *pdf* scales 1–70 | | | | | |
| **Average Values** | 53.1 | 46.11 | 47.69 | 52.31 | 53.89 |

**Table 1** (*continued*)

| Combination L M H Images | | | | | |
|---|---|---|---|---|---|
| SVM classifier | %CC | %FP | %FN | %SE | %SP |
| SVM rbf spread = 6.4 | 71.90 | 43.07 | 13.14 | 86.86 | 56.93 |
| **PCA** for *pdf* scales (Low: 1,2,3,4,5,6) (Med: 3,4,9,11,12) (High: 19,12,15,11,18,2) | | | | | |
| SVM rbf spread = 6.4 | 71.90 | 45.26 | 10.95 | 89.05 | 54.74 |
| *pdf* scales (Low: 1,2,3,4,5,6) (Med: 3,4,9,11,12) (High: 19,12,15,11,18,2) | | | | | |
| SVM rbf spread = 12.8 | 69.34 | 43.80 | 17.52 | 82.48 | 56.20 |
| **PCA** for *cdf* scales 1–210 | | | | | |
| SVM rbf spread = 2.2627 | 71.90 | 39.42 | 16.79 | 83.21 | 60.58 |
| *cdf* scales 1–210 | | | | | |
| SVM rbf spread = 9.0510 | 70.80 | 42.34 | 16.06 | 83.94 | 57.66 |
| **PCA** for *pdf* scales 1–210 | | | | | |
| SVM rbf spread = 6.4 | **73.36** | **39.42** | **13.87** | **86.13** | **60.58** |
| *pdf* scales 1–210 | | | | | |
| **Average Values** | 71.53 | 42.22 | 14.72 | 85.28 | 57.78 |
| Combination L M H Images | | | | | |
| PNN classifier | %CC | %FP | %FN | %SE | %SP |
| PNN spread = 5 | 69.34 | 53.28 | 8.03 | 91.97 | 46.72 |
| **PCA** for *pdf* scales (Low: 1,2,3,4,5,6) (Med: 3,4,9,11,12) (High: 19,12,15,11,18,2) | | | | | |
| PNN spread = 5 | 69.71 | 54.01 | 6.57 | 93.43 | 45.99 |
| *pdf* scales (Low: 1,2,3,4,5,6) (Med: 3,4,9,11,12) (High: 19,12,15,11,18,2) | | | | | |
| PNN spread = 5 | 69.71 | 37.96 | 22.63 | 77.37 | 62.04 |
| **PCA** for *cdf* scales 1–210 | | | | | |
| PNN spread = 5 | 68.61 | 40.15 | 22.63 | 77.37 | 59.85 |
| *cdf* scales 1–210 | | | | | |
| PNN spread = 5 | **70.44** | **42.34** | **16.79** | **83.21** | **57.66** |
| **PCA** for *pdf* scales 1–210 | | | | | |
| PNN spread = 5 | **70.07** | **38.69** | **21.17** | **78.83** | **61.31** |
| *pdf* scales 1–210 | | | | | |
| **Average Values** | 69.65 | 44.41 | 16.3 | 83.7 | 55.6 |

Returning to the established clinical knowledge on the stability of atherosclerotic plaques, we note that the $L$-images capture the lipid content (as well as other non-lipid structures: thrombus, blood or haemorrhage). Thus, to the extend that these $L$-images reflect lipid content, it is clear that we would expect that pattern spectra that are highly concentrated at the lower scales would also characterize stable, asymptomatic plaques. Again, this is in agreement with the clinical finding that large lipid cores are found in unstable plaques while small lipid concentrations are found in stable plaques [18]. A careful inspection of the $L$-images of Figs. 3 and 5 shows a dramatic demonstration of how this information is captured in the PDF. Clearly, the asymptomatic plaques have a "spiky" PDF concentrated in the lower scales, while the symptomatic plaques gave a significant PDF spread over all scales. Also, note that the PDF spread of the symptomatic plaques is consistent with the presence of large lipid cores. To further recognize the clinical significance of this finding, we note that our medical team has decided to use the pattern spectra of these $L$-images in the routine clinical exams to screen patients for the presence of symptomatic plaques.

In contrast, we may expect large components in the $H$-images to reflect plaque stability. This comes from the fact that $H$-images capture calcified and collagen components that are unlikely to rupture [18]. However, it is also important to note that plaque instability does not account for significant stenosis where a stable plaque will not rupture, but will grow to disrupt blood supply. In any case, in Figs. 3 and 7, we can see that the PDFs of the asymptomatic plaques are somewhat more spread-out than for the symptomatic plaques. In Fig. 7, it is also clear that

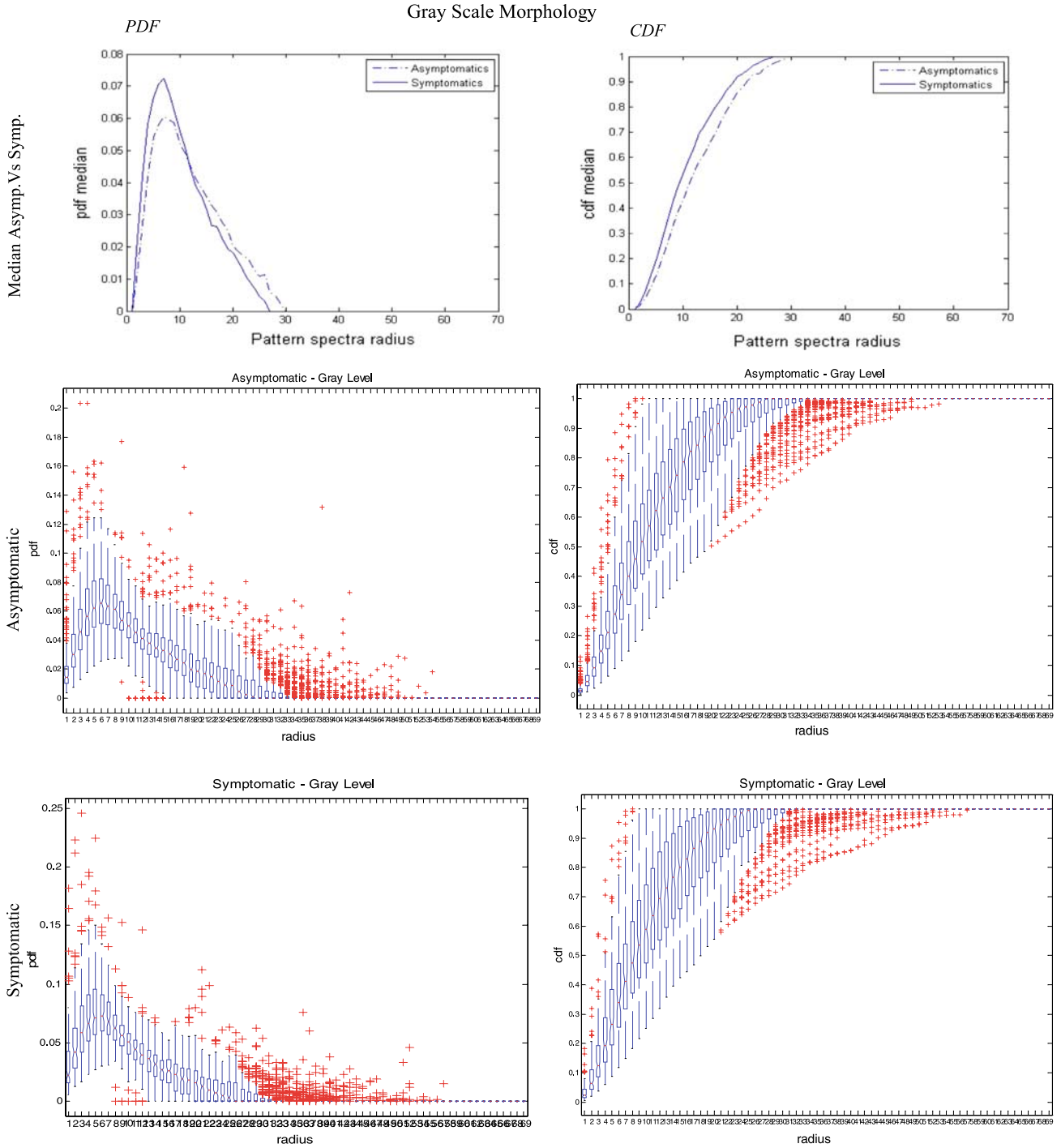


**Fig. 8** **a** Median probability density function *(pdf)* and cumulative distribution function *(cdf)* plots for the pattern spectra of gray scale images; symptomatic plot is plotted with a *solid line* while the asymptomatic one with a *dotted line*. **b** Box plots of *pdf* and *cdf* for the asymptomatic carotid plaques. **c** Box plots of *pdf* and *cdf* for the symptomatic carotid plaques

asymptomatic outliers occur at very high scales as compared to much fewer such outliers in the asymptomatic plaques.

In the specific example of Fig. 1 we can see how the solid components in the $L$-image are indicative of plaque instability. The hypoechoic components of the symptomatic plaque of Fig. 1 will clearly produce a large number of components in its PDF decomposition. Furthermore, it is important to recognize the lack of any large components in the $H$-image of the lower half of the symptomatic plaque. Based on current clinical knowledge, we would expect that the lower-half of the symptomatic plaque will rupture, especially since it is

**Table 2** Percentage of correct classifications (%CC), percentage of false positives (%FP), percentage of false negatives (%FN), percentage sensitivity (%SE) and percentage specificity (%SP) of Gray Scale morphological features using the SVM and PNN classifiers. Classification models developed for two classes using the leave one out method, and 137 symptomatic and 137 asymptomatic plaques

| Gray Scale | | | | | |
|---|---|---|---|---|---|
| SVM classifier | %CC | %FP | %FN | %SE | %SP |
| SVM rbf spread = 2.2627 | **66.79** | 20.44 | 45.99 | 54.01 | 79.56 |
| **PCA** for *pdf* scales 2,3,5,10,21,23 | | | | | |
| SVM rbf spread = 0.5657 | 65.33 | 28.47 | 40.88 | 59.12 | 71.53 |
| *pdf* scales 2,3,5,10,21,23 | | | | | |
| SVM rbf spread = 2.2627 | 63.14 | 42.34 | 31.39 | 68.61 | 57.66 |
| **PCA** for *cdf* scales 1–70 | | | | | |
| SVM rbf spread = 2.2627 | 62.41 | 32.12 | 43.07 | 56.93 | 67.88 |
| *cdf* scales 1–70 | | | | | |
| SVM rbf spread = 1.1314 | 60.22 | 43.80 | 35.77 | 64.23 | 56.20 |
| **PCA** for *pdf* scales 1–70 | | | | | |
| SVM rbf spread = 0.5657 | **63.14** | **36.50** | **37.23** | **62.77** | **63.50** |
| *pdf* scales 1–70 | | | | | |
| **Average Values** | 63.51 | 33.95 | 39.06 | 60.95 | 66.06 |
| Gray Scale | | | | | |
| PNN classifier | %CC | %FP | %FN | %SE | %SP |
| PNN spread = 5 | 56.57 | 22.63 | 64.23 | 35.77 | 77.37 |
| **PCA** for *pdf* scales 2,3,5,10,21,23 | | | | | |
| PNN spread = 5 | 56.57 | 22.63 | 64.23 | 35.77 | 77.37 |
| *pdf* scales 2,3,5,10,21,23 | | | | | |
| PNN spread = 5 | 60.58 | 36.50 | 42.34 | 57.66 | 63.50 |
| **PCA** for *cdf* scales 1–70 | | | | | |
| PNN spread = 5 | **62.04** | **35.77** | **40.15** | **59.85** | **64.23** |
| *cdf* scales 1–70 | | | | | |
| PNN spread = 5 | 58.76 | 42.34 | 40.15 | 59.85 | 57.66 |
| **PCA** for *pdf* scales 1–70 | | | | | |
| PNN spread = 5 | 60.22 | 48.91 | 30.66 | 69.34 | 51.09 |
| *pdf* scales 1–70 | | | | | |
| **Average Values** | 59.12 | 34.8 | 46.96 | 53.04 | 65.2 |

most likely composed of a large lipid core with little collagen or calcium to hold it together.

Based on our discussion, we can see that low-scales from the $L$-images and higher-scales from the $H$-images should lead to the best combinations of morphological features. This is clearly demonstrated in the selected scales of Table 1. For the $L$-images, the best scales were found to be the lowest possible: 1–6 while all-but one of the best scales for the $H$-images were found to be for scales that are larger than 10. As mentioned in the results section, we select morphological scales using the decision trees algorithm after PCA. Thus, the resulting scales that were selected provide the largest discriminatory power from the pattern spectra that captured most of the variance.

Compared to multi-level morphology, we find it a little harder to relate the results from gray-scale morphology to our clinical understanding of unstable plaques. Part of the problem is surely due to the complexity of the different components. A comparative example is given in Fig. 2. After a careful inspection, it can be seen that the effect of grey scale morphology is to "flatten-out" the different plaque components, by producing large plaque components with lower image intensity. Here, we recall that in the limit, the openings will generate the zero-image. Clinically, we expect that heterogeneous plaques will be the symptomatic ones. Returning to the example in Fig. 2, homogeneous plaques will be characterized by uniform intensity regions. These large regions will thus be expected to spread the pattern spectrum

over the larger scales. Thus, symptomatic pattern spectra will tend to dominate the asymptomatic pattern spectra over the larger scales. Furthermore, since the spectra are normalized, this would imply that the asymptomatic pattern spectra will remain below the symptomatic pattern spectra at the lower scales. This is clearly reflected in the PDF plots of Figs. 4 and 8. On the other hand, in comparison, the morphological decomposition of the $L$-image appears much more effective, with significant binary components being removed at different sizes.

We can confirm that the appropriate scales were selected to separate between the symptomatic and asymptomatic plaques by comparing the average and median spectra in Figs. 4 and 8. It is clear that the selected PCA components around 10, 21, 23 reflect strong separations between the average and median spectra (recall that plaques are collected at 20 pixels per mm, and thus, scale = 20 corresponds to 1 mm).

Between the Grey-scale PDF plots of Fig. 4 and the $L$-image plots of Fig. 3, we can clearly see that the $L$-images provided much better separations. This also explains the better performance achieved through the use of the $L$-image spectra.

## 6 Conclusions

The primary motivation behind this study was in the development of morphological image analysis methods that have strong connections to prior clinical studies on what constitutes an unstable, symptomatic plaque. The clinical motivations for the analysis was outlined in Sect. 1.2 and the clinical connections were also made in the discussion of the results in Sect. 5.3. Here, we note that the $L$-images alone gave results that are slightly better than complicated multi-feature multi-classifier systems (73.7% versus 73% of [5], also see [4]).

However, a significant advantage of the study is that we believe that there is a clear clinical explanation of why the pattern spectra for $L$-images performed best. The $L$-images capture the lipid components of the plaques (among other components). From our clinical understanding of unstable plaques, unstable plaques have large lipid components while stable plaques have small lipid components. By examining the average (and median) pattern spectra for symptomatic and asymptomatic plaques, we can infer that pattern spectra for the $L$-images must have captured this clinical fact. Thus, our medical team has decided to use the pattern spectra for the $L$-images in all future screening for symptomatic plaques.

While our paper attempted to motivate the computational analysis from a more clinical perspective, it is important to outline some of the limits of our approach. Our focus on morphological features, as well as our prior focus on common texture features, does not incorporate diagnostic information regarding stenosis. Furthermore, we have not incorporated any obvious clinical factors such as smoking habits and cholesterol levels. From the biomedical engineering perspective, future studies will have to investigate the correspondence between non-invasive, 3D, multi-modality imaging methods and 3D histological exams to develop hybrid segmentation methods for segmenting out the various plaque components (lipid, fibrous, blood, etc.). Then, 3D geometrical models can be used to measure the different structural components of the plaques. Following such an approach, we will then want to measure the stress distributions over the plaques, together with the materials that these stresses are applied to. This approach will surely provide greater insight into what causes plaques to rupture.

**Acknowledgements** This work was funded through the project Integrated System for the Evaluation of Ultrasound Imaging of the Carotid Artery (TALOS), of the Research Promotion Foundation of Cyprus.

## References

1. Belcaro G, Nicolaides AN, Laurora G et al (1996) Ultrasound morphology classification of the arterial wall and cardiovascular events in a 6-year follow-up study. Arterioscler Thromb Vasc Biol 16:851–856
2. El-Barghouti N, Nicolaides AN, Tegos T et al (1996) The relative effect of carotid plaque heterogeneity and echogenicity on ipsilateral cerebral infarction and symptoms of cerebrovascular disease. Int Angiol 15:300–306
3. Arnold JAC, Modaresi KB, Thomas N et al (1999) Carotid plaque characterization by duplex scanning. Observer error may undermine current clinical trials. Stroke 30:61–65
4. Wilhjelm JE, Gronholdt LM, Wiebe B, Jespersen SK, Hansen LK, Sillesen H (1998) Quantitative analysis of ultrasound B-mode images of carotid atherosclerotic plaque: correlation with visual classification and histological examination. IEEE Trans Med Imaging 17(6):910–922
5. Christodoulou CI, Pattichis CS, Pantziaris M, Nicolaides A (2003) Texture based classification of atherosclerotic carotid plaques. IEEE Trans Med Imaging 22:902–912
6. Christodoulou CI, Kyriacou E, Pattichis MS, Pattichis CS, Nicolaides A (2003) A comparative study of morphological and other texture features for the characterization of atherosclerotic carotid plaques. In Proceedings of CAIP 2003, The Nederlands, pp 165–173
7. Christodoulou CI, Pattichis CS, Kyriacou E, Pattichis MS et al (2005) Ultrasound imaging in the assessment of carotid plaque morphology. In: Costaridou L (ed) Applied medical image analysis methods. CRC Press, Boca Raton, pp 87–135
8. Kyriacou E, Pattichis MS, Christodoulou C, Pattichis CS, Kakkos S, Nikolaides A (2005) Ultrasound imaging in the analysis of carotid plaque morphology for the assessment of stroke. In: Suri JS, Yuan C, Wilson DL, Laxminarayan S (eds) Plaque characterization using multimodality imaging: pixel to molecular. IOS, Amsterdam, pp 241–275
9. Kyriacou E, Pattichis M, Christodoulou C, Pattichis C, Kakkos S, Nicolaides A (2005) Multiscale morphological analysis of the atherosclerotic carotid plaque. In: Proceedings of the 27th annual international conference IEEE EMBS, Shanghai, China

10. de Bray JM, Baud JM, Dauzat M (1997) Consensus concerning the morphology and the risk of carotid plaques. Cerebrovasc Dis 7:289–296
11. Thiele BL, Jones AM, Hobson RW et al (1992) Standards in noninvasive cerebrovascular testing. J Vasc Surg 15:995–1003, Report from the committee on standards for noninvasive vascular testing of the Joint council of the society for vascular surgery and the North American chapter of the international society for cardiovascular surgery
12. Reilly LM, Lusby RJ, Hughes L et al (1983) Carotid plaque histology using real-time ultrasonography. Clinical and therapeutic implications. Am J Surg 146:188–193
13. Johnson JM, Kennelly MM, Decesare D et al (1985) Natural history of asymptomatic carotid plaque. Arch Surg 120:1010–1012
14. Langsfeld M, Gray-Weale AC, Lusby RJ (1989) The role of plaque morphology and diameter reduction in the development of new symptoms in asymptomatic carotid arteries. J Vasc Surg 9:548–557
15. Polak JF, Shemanski L, O'Leary DH et al (1998) For the cardiovascular health study. Hypoechoic plaque at US of the carotid artery: an independent risk factor for incident stroke in adults aged 65 years or older. Radiology 208:649–654
16. AbuRahma AF, Thiele SP, Wulu JT Jr (2002) Prospective controlled study of the natural history of asymptomatic 60% to 69% carotid stenosis according to ultrasonic plaque morphology. J Vasc Surg 36:1–6
17. Sterpetti AV, Schultz RD, Feldhaus RJ et al (1988) Ultrasonographic features of carotid plaque and the risk of subsequent neurologic deficits. Surgery 104:652–660
18. Davies MJ (1997) The composition of coronary artery plaques. New Engl J Med 336:1312–1314
19. Elatrozy T, Nicolaides A, Tegos T et al (1998) The objective characterisation of ultrasonic carotid plaque features. Eur J Vasc Endovasc Surg 16:223–230
20. Sabetai MM, Tegos TJ, Nicolaides AN et al (2000) Reproducibility of computer-quantified carotid plaque echogenicity. Can we overcome the subjectivity? Stroke 39(9):2189–2196
21. Tegos TJ, Sametai MM, Nicolaides AN et al (2000) Comparability of the ultrasonic tissue characteristics of carotid plaques. J Ultrasound Med 19:399–407
22. Loizou C, Pattichis C, Istepanian R, Pantziaris M, Nicolaides A (2004) Atherosclerotic Carotid Plaque Segmentation. In: Proceedings of the 26th annual international IEEE EMBS conference, San Francisco, USA
23. Dougherty ER (1992) An introduction to morphological image processing. SPIE Optical Engineering Press, Belligham
24. Maragos P (1989) Pattern spectrum and multiscale shape representation. IEEE Trans Pattern Anal Mach Intell 11:701–715
25. Specht DF (1990) Probabilistic neural networks. INNS Neural Netw 3(1):109–118
26. Joachims T (1999) Making large-scale SVM learning practical. In: Schölkopf B, Burges C, Smola A (eds) Advances in kernel methods—support vector learning. MIT, Cambridge, Chap 11
27. Ebrchart RC, Dobbins RW (1990) Neural networks PC tools a practical guide. Academic Press, New York
28. Mavrommatis A (2006) Morphology of carotid US images. MSc thesis, University of Cyprus, Nicosia, Cyprus
29. Panagiotou S (2006) Classification of plaques using SVM class. MSc thesis, University of Cyprus, Nicosia Cyprus
30. Han J, Kamber M (2000) Data mining: concepts and techniques. Kaufmann, Los Altos